Journal of Rock Mechanics and Geotechnical Engineering 17 (2025) 5111–5121

Contents lists available at ScienceDirect

Journal of Rock Mechanics and Geotechnical Engineering

journal homepage: www.jrmge.cn

Full Length Article

Synchrotron-radiation computed tomography of the water drop penetration time test on hydrophobic soils

Clara M. Toffoli [a,*], Marius Milatz [b], Julian P. Moosmann [c], Thomas Jentschke [c], Felix Beckmann [c], Jürgen Grabe [a]

[a] Institute of Geotechnics and Construction Management, Hamburg University of Technology, Hamburg, 21079, Germany
[b] Institute of Geomechanics und Geotechnics, Braunschweig University of Technology, Braunschweig, 38106, Germany
[c] Helmholtz-Zentrum Hereon, Geesthacht, 21502, Germany

ARTICLE INFO

Article history:
Received 7 June 2024
Received in revised form
28 April 2025
Accepted 10 June 2025
Available online 20 June 2025

Keywords:
Hydrophobic soil
Synchrotron tomography
Water drop penetration time (WDPT) test

ABSTRACT

The water drop penetration time (WDPT) test consists of placing water drops on a material's surface in order to evaluate how long it takes to penetrate the pores. It is used to evaluate the hydrophobicity of materials. This study aims at investigating in more detail the soil-water interaction during the test, exposing its mechanism. For that, a model soil named Hamburg Sand was coated with a hydrophobic fluoropolymer and then a WDPT test was performed while computed tomography (CT) images were taken. Tomography experiments were performed at the P07 high-energy materials science (HEMS) beamline, operated by Helmholtz–Zentrum Hereon, at the storage ring PETRA III at the Deutsches Elektronen-Synchrotron (DESY) in Hamburg. Using synchrotron radiation, a tomogram can be obtained in about 10 min, way less time than regular laboratory X-ray sources usually owned by universities. The faster imaging enables the observation of the drop penetration during time and thus provides insight into the dynamics of the process. After that, digital discrete image correlation is performed to track the displacement of the grains throughout time. From the results one can observe that, as the drop is absorbed at the material's surface, the grains directly around the droplet base are dragged to the liquid-air interface around the drop, revealing grain kinematics during capillary interactions of the penetrating liquid and sand grains.

1. Introduction

The objective of this study is to investigate in more detail the mechanism of the water drop penetration time (WDPT) test for hydrophobic granular material, looking into the displacement of the grains in contact with the droplet and its penetration. It can be observed with the naked eye in the geotechnical laboratory that grains of the sand surface tend to climb around the water droplet, on the interface between droplet and air, while it penetrates. As a confirmation, this behaviour is noticed in Fig. 1. To confirm the inference and quantify these displacements of the grains induced by the droplet, sequential computed tomography (CT) images were obtained while the droplet penetrates the hydrophobic sand substrate and then analysed. Given the time frame of the phenomenon, synchrotron-radiation CT has to be employed in order to be able to scan the sample with high enough resolution and in short enough time span.

Hydrophobic soil resists the penetration of water on its surface, making it possible for a droplet of water to rest on the surface of sand, for example, as presented in Fig. 1. The blue colour of the droplet in the figure is produced with food colouring only for visualisation purposes. From this distinct hydro-mechanical behaviour stems the resistance to water penetration that allows specific applications in Geotechnical engineering, e.g. covering of slope or landfill surface (Wijewardana et al., 2015; Zheng et al., 2021); covering of tailings dam for their closure; construction of pavement layers, in which the amount of moisture is reduced underneath the asphalt layer and thus the consequences of freezing as well (DeBano, 1981). Other recent studies in the field of hydrophobic soils confirming its currentness but not totally related to this study are, for example, Bayad et al. (2020), Al-Atroush and Sebaey (2021),

* Corresponding author.
E-mail address: clara.toffoli@tuhh.de (C.M. Toffoli).
Peer review under responsibility of Institute of Rock and Soil Mechanics, Chinese Academy of Sciences.

https://doi.org/10.1016/j.jrmge.2025.06.003

Fig. 1. Coloured water droplet resting on the surface of hydrophobic sand.

Karatza et al. (2021), and Sandor et al. (2021).

The definition of a hydrophobic material stems from the contact angle in the triple-line, between water, air and soil, or any other component that is present in the region of interest, as indicated by θ in Fig. 2. By definition, an angle larger than 90° indicates a hydrophobic substrate, while one smaller than that characterises a hydrophilic material. The angle is measured by the sessile drop method, using a contact angle goniometer, a device that contains a pipette, able to place a fixed volume droplet on the material surface, and also a camera, that registers the evolution of the contact angle with time (Bachmann et al., 2000). On this technique the droplet is placed on a single layer of grains, fixed by glue to a glass plate, and thus grains do not move from their original position.

In this context it is important to point out the difference between intrinsic contact angle and the one measured at a surface composed of grains of different materials, like sand. The intrinsic contact angle measurement is achieved on pure smooth mineral surfaces, which are very different from real soils and rocks. There, many factors can affect the angle, such as surface morphology, mineralogy, chemical equilibrium between phases, fluid distribution etc. For the measurement in sand, the procedure described in Bachmann et al. (2000) is employed: A single-grain layer of sand is glued on a glass plate by means of a double-sided adhesive tape.

Regarding the origination of hydrophobic materials, hydrophobic soils are usually obtained when grains are coated with a hydrophobic substance, either in an intended or unintended manner, given that the naturally encountered minerals, frequently employed in Geotechnics, are usually hydrophilic (Lourenço et al., 2015). In nature hydrophobic soils stem from the coating of individual particles by organic hydrophobic components, that can originate in substances produced by plants, by microorganisms, from contamination or fires (Bardet et al., 2014). Hydrophobic soils can be also created artificially using a hydrophobic coating imposed to the particles. In geotechnical studies this is usually achieved via a process named silanization, where the sample is immersed in a chemical compound of the silane family (Liu and Lourenço, 2021). In this paper the hydrophobic coating is executed with a fluorpolymer and a different technique, namely cold plasma polymerisation. Although the hydrophobic coating can also affect the dry mechanical behaviour of the material (Liu et al., 2019a, b; Liu and Lourenço, 2021), it will not be addressed in this paper.

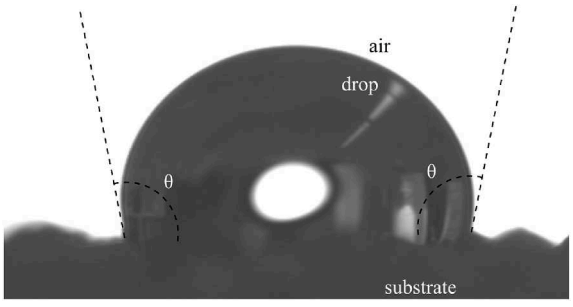

Fig. 2. Contact angle of a droplet resting on hydrophobic sand monolayer.

In order to measure how hydrophobic a granular material is, different tests are available. The water drop penetration time (WDPT) test, topic of this paper, consists of placing droplets of water with standardised volume on the surface of the granular material and measuring how long they take to fully penetrate the sample. Its result is the averaged time of penetration of all applied droplets, which is compared to classification criteria (Doerr, 1998). The standard deviation of the measures obtained for this test can be up to 600 s (Lin and Lourenço, 2020). As a completely hydrophobic material would have an infinite penetration time, the fact that the drop penetrates after a time interval indicates that the soil water repellency (SWR) can decrease as the material is saturated. As the contact angle describes the hydrophobicity magnitude, the WDPT relates to its persistence (Lin and Lourenço, 2020). A "critical saturation degree" can therefore be determined to separate the hydrophobic and hydrophilic behavior of the material. This classification, though, can also be established based on different criteria, according to the following items. As this test qualifies and not quantifies the hydrophobicity of a material, it can be classified as an index test. Two tests that measure the hydrophobicty magnitude are the sessile drop method (SDM), already described above, and the ethanol percentage (EP), which consists in mixing water and ethanol in different percentages to get solutions with different surface tension and testing from which concentration the solution does not penetrate the sample anymore.

Doerr (1998) describes the variations in the procedure of the WDPT and its classification criteria found in literature, reproduced in this paper on Table 1 (Adams et al., 1970; Roberts and Carbon, 1971; McGhie and Posner, 1981; Ma'shum and Farmer, 1985; Bisdom et al., 1993; Doerr et al., 1996). Since there is no standard procedure for it, different researchers developed different evaluation criteria. For longer times, the droplet evaporation starts influencing the test significantly. They also propose a standardisation of the test, particularly of the quantity of applied droplets, which shall be 5 or 15, and the temperature during the experiment, which shall be 20° Celcius. Although Doerr (1998) suggest producing the droplet with a hypodermic syringe, one can note that a laboratory pipette is a better way to produce droplets with constant volume.

Regarding computed tomography, this is a tool frequently employed in the field of geotechnics (e.g. Shahraeeni and Or, 2012; Milatz et al., 2021; Wang et al., 2021). The main advantage is the possibility of observing and following individual grains during the occurrence of a phenomenon of interest without interferring or destroying the sample.

2. Methodology

In order to be able to track grain displacement during the penetration of the water droplet in the hydrophobic substrate, synchrotron-radiation CT was employed. The following sub sections describe in more detail the preparation of the hydrophobic sand, the execution of the WDPT test, of the CT images and also the processing of the CT data to obtain the displacement field.

2.1. Sand hydrophobization: Cold plasma coating

The base substrate sand used for this study is Hamburg sand, a model soil employed frequently at the Hamburg University of Technology, where the tests were planned. It has a grain density of

Table 1
Threshold WDPT in seconds and the respective hydrophobicity degrees according to different authors (Doerr, 1998).

Classification	Adams et al. (1970)	Bisdom et al. (1993)	Doerr et al. (1996)	Ma'shum and Farmer (1985)	McGhie and Posner (1981)	Roberts and Carbon (1971)
Hydrophilic	<10	<5	<60	<1	<60	<1
Slightly hydrophobic	10–60	5–60	–	–	–	1–10
Strongly hydrophobic	–	60–600	–	–	–	10–60
Severely hydrophobic	>60	600–3600	–	–	–	>60
Extremely hydrophobic	–	>3600	>3600	–	–	–

2.64 g/cm^3, a d_{10} of 0.45 mm, a d_{50} of 0.68 mm, and a d_{max} of 2.00 mm. The maximum void ratio is 0.805, while the minimum is 0.520.

The hydrophobic coating is based on a hydrophobic polymer, namely PFA-C6 (1H,1H,2H,2H-perfluorooctylacrilate), which has an extremely low surface energy. The structure of the molecule is presented in Fig. 3. To coat the sand, it is air dried and then inserted together with the monomer of the polymer in a cold plasma chamber and kept there for a fixed amount of time. The corresponding liquid monomer of this polymer is injected into this chamber with a flow rate of 30 μL per minute by a dosing pump. A pre-treatment with oxygen can be employed to facilitate the absorption of the coating. This process leads to the deposition of a monolayer of the organic polymer, which gets absorbed to the initially hydrophilic surface (Maciejewski et al., 2015; Zainal et al., 2015; Ahmad et al., 2018; Schroeter et al., 2021). Teng (2012); Henry et al. (2018) described other possible coating fluoropolymers and their development in the industry.

For more detail about the coating process parameters and their influence on the hydrophobicity and behaviour of the coating when exposed to simulated field conditions, see Toffoli et al. (2023). Considering the naming of the different types of coated Hamburg sand in the previously cited paper, one of the samples used in this paper consists of "material V7" and the other, "material V8". Material V7 is kept in the plasma chamber for 60 min without pre-treatment, while material V8 is kept in the chamber for 20 min after receiving an oxygen pre-treatment. Regarding the hydrophobicity classification according to the WDPT, the materials are both extremely hydrophobic in the classification of Doerr et al. (1996) in Table 1, given that a droplet rests on its surface for longer than 3600 s. In this paper two different samples were scanned, hereinafter referred to as samples 1 and 2. Both of them consist of coated Hamburg Sand, the coating being the only difference between samples. From the terminology in Toffoli et al. (2023), sample 1 consists of "material V7", while sample 2 is "material V8".

Although it would be valuable for this study to observe the mechanism also in perfectly round grains, namely soda-lime glass beads, and compare the observations to the behavior of real irregularly shaped sand grains described in this paper, this material did not perform sufficiently in preliminary tests presented in Toffoli et al. (2023). As discussed in the reference, materials V4 and V5, as by the naming used by the authors there, are comparatively less hydrophobic than the sand samples and also loose most of their hydrophobicity after six months. A different strategy is necessary to hydrophobize this material.

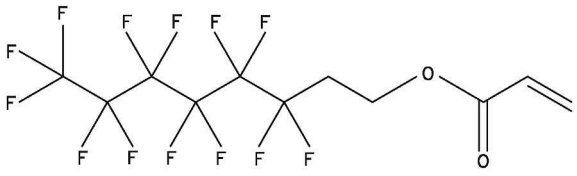

Fig. 3. Molecular structure of 1H,1H,2H,2H-perfluorooctylacrilate.

Hydrophobic coating with this type of fluoropolymers is also highly employed in other fields, e.g. icing control in aerospace industry (Keley, 2017), manufacturing of hydrophobic textiles (Yang et al., 2023), creation of medical devices (Matsuoka et al., 2021) and manufacturing of non sticking food related instruments (Magens et al., 2017). To the best knowledge of the authors, the use of this technique and chemicals to hydrophobize sand is not yet described in literature.

Although the aimed hydrophobic effects are obtained by this technique, one of its downsides is the current price of executing it, which can make it unattractive to industrial scale. The energy consumption of the plasma chamber is one of its reasons. Another possible disadvantage is that the use of the method could lead to environmental contamination, given that the manufacturing of the coating chemicals can be the cause of air and top soil layer contamination (Dauchy, 2023). Furthermore, the washing of the coating by the groundwater when the material is employed in the field could be observed (Thepaksorn et al., 2023). Henry et al. (2018) presents, though, toxicity data of per- and polyfluoroalkyl substances (PFAS), indicating that it can be classified as a "polymers of low concern" (PLC) and thus shall not be treated as a regular polymer for regulatory purposes.

2.2. WDPT test

As described in the sections above, the WDPT test consists of placing droplets of deionised water on the surface of hydrophobic material and timing how long it takes them to fully penetrate it. For the scanned test, a 30 μL droplet was used, a decision based on the size of the sample and the sample holder. This value is around the ones usually seen in the literature: 60 μL in Lourenço et al. (2015, 2018), 40 μL in Bayad et al. (2020), no exact number because it was done with a hypodermin syringe in Doerr (1998). There is no standardization of this volume though.

A laboratory pipette with a 10–100 μL range was employed to produce droplets with a more precise volume. Given that the imaged area is small, only one droplet could be placed, in disagreement with the practice of placing more than one and averaging the time they take to fully penetrate the sample.

The 30 μL droplet is significantly bigger than the individual sand grains, enabling the described phenomena to occur. Assuming spherical grains and considering the grain diameter at 50% passing (d_{50}) of 0.68 mm, the volume of one single grain is around 0.7 mm^3, meaning around 43 times smaller than the droplet.

Regarding temperature, both tests were done at room temperature, that was around 24° Celcius, and no further investigation of the influence of higher or lower temperature was done so far. Since the viscosity of water is highly affected by temperature, this factor could have a significant influence on the behavior.

2.3. Synchrotron computed tomography imaging

The μCT scans were conducted at the High Energy Materials Science (HEMS) Beamline P07 of PETRA III, operated by Helmholtz-Zentrum Hereon at Deutsches Elektronen-Synchrotron (DESY) in Hamburg, Germany. Both conventional absorption and phase contrast imaging were employed at a sample-detector distance of

$z = 0.2$ m. A total of 5101 projections were acquired from a 180° fly-scan. Prior to the experiment, a simulation was performed using mesh objects created from segmented data of previous experiments. This simulation helped optimize the contrast between background and water, as their contrast is significantly lower compared to that of sand and glass beads. The optimal photon energy determined by the simulation was $E_{sim} = 40$ keV. However, in the actual experiment, a slightly higher photon energy of $E_{exp} = 44$ keV was selected to mitigate the risk of radiolysis and enhance phase contrast. Since the condensation processes observed were relatively slow compared to the tomographic scan time, a longer exposure time of $t_{exp} = 60$ ms was chosen to ensure high image quality for subsequent analysis. Photon detection was carried out using an indirect detector system comprising a CdWO4 scintillator and a CCD-equipped camera. The acquired images had a resolution of 7919 × 3000 pixels, with an effective pixel size of $ps_{eff} = 0.92$ μm due to the optical system's fivefold magnification. A raw binning of four was applied. Phase retrieval was performed using the linearised transport of intensity equation (TIE), followed by tomographic reconstruction via Filtered Backprojection with a Ram-Lak filter. The reconstruction workflow and analysis tools provided by HEMS were utilised for data processing (Moosmann et al., 2014; Moosmann, 2019). For processing of the data, binning of two had to be applied.

After placing the droplet with the pipette on the surface of the hydrophobic granular material, sequential tomograms were obtained. Sample 1 was scanned five times, while sample 2 was scanned nine times. The tomograms correspond to time steps, and each of them contains 299 horizontal slices after binning. Since each scan takes around 10 min while employing the settings described above, each time step corresponds to a difference in time of 10 min. A possible limitation of this study is the fact that only two samples were imaged. Although the mechanism of the water droplet penetration time test for hydrophobic granular material is evident in these samples, the analysis of more samples could lead to a more complete study. This was not possible given the time limitations inherent to synchrotron beamtimes.

2.4. Tracking of grain displacement

The first step to create a displacement field of grains via discrete digital image correlation (DDIC) (Hall, 2012) is labelling the grains, so that they can be tracked from one tomogram to the next. Traditionally, only the first tomogram is labelled, and those labelled grains are tracked through all time steps. For that, the obtained displacement field between steps, i.e. 1 and 2 is applied to the labels in order to use them to find the displacements of the grains between steps, i.e. 2 and 3. Because of the small dimensions of the imaged field, most of the grains were not fully imaged, making it impossible to use this approach. In different steps, slightly different parts of the grains were imaged, preventing the analysis to converge for some labels, meaning that the labels corresponding to those problematic partially imaged grains must be deleted for the analysis to succeed. For this reason, different stacks have small differences in which grains could be labelled and thus it was not possible to track all grains/labels in all steps. Each tomogram corresponding to a time step had to be labelled independently, and the displacement field was calculated afterwards subsequently employing those labels. The labelling and related operations were done using ImageJ (Schindelin et al., 2012) and an associated plugin named MorphoLibJ (Legland et al., 2016).

It is important to highlight that those removed labels are not in the interest region around and on top of the droplet, but rather at the base of the sample, where more grains are present, closer to each other. Those grains have a very small or nonexistent displacement, since they are outside of the zone of influence of the droplet.

After the labels were available for stack n, the steps of the methodology for performing the DDIC using the software spam (Stamati et al., 2020) is:

1. perform a *spam* pixel search from stack n to $n+1$;
2. perform a *spam* DDIC from stack n to $n+1$ using as initial guess of the ϕ field calculated at the pixel search, with the ϕ field being the field of functions correlating the initial position and position in space at time t of the discrete elements being analysed;
3. filter the obtained ϕ field with spam function *filterPhiField* by averaging ϕ of neighbours;
4. perform a *spam* DDIC from stack n to $n+1$ using the filtered ϕ field from step 3;
5. in case that the analysis of one or two grains still does not converge, a *spam* eye registration step is performed for those grains only and the obtained ϕ is used as initial guess for a last DDIC performed on those single grains only.

After those steps, the displacement field was available for the labelled grains of all stacks.

3. Results and analyses

3.1. Greyscale images

Fig. 4 presents the central vertical greyscale slices of time steps one and five of sample 1, while Fig. 5 presents the central vertical greyscale slices of time steps one and nine of sample 2. After placing the droplet it is necessary to search the beam room, close its isolation door and go to the control room to start the image obtainment. Around 2 min are needed for those steps. Knowing also that each scan takes around 10 min to be performed, it can be inferred that the state observed is from half this time, meaning that time step 1 is obtained at 7 min (2 plus 5), time step 2 from 17 min (7 plus 10), time step 3 from 27 min (17 plus 10) and so on. Also, in Figs. 4b and 5b, it is noticeable that both droplets remained partially on the surface of the samples after the imaging was complete, given their high degree of hydrophobicity.

All images obtained at this beamtime were published in Toffoli et al. (2024). In Figs. 4 and 5 it is already noticeable that the grains have the tendency of “climbing” the droplet and rotating, which will be quantitatively analysed in this paper. Given the motion

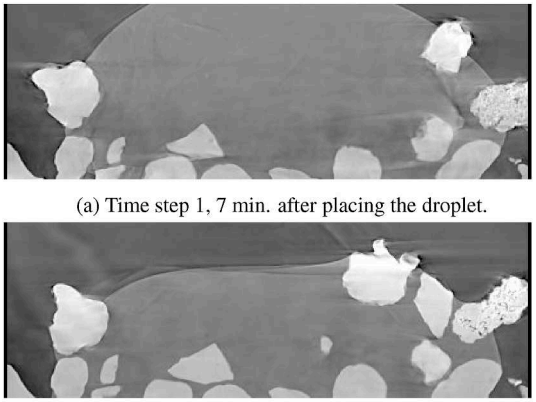

(a) Time step 1, 7 min. after placing the droplet.

(b) Time step 5, 47 min. after placing the droplet.

Fig. 4. Greyscale vertical radial slices of tomogram corresponding to time steps 1 (a) and 5 (b) of the penetrating droplet in sample 1.

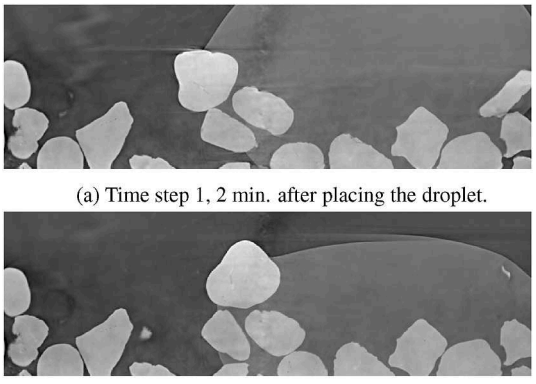

(a) Time step 1, 2 min. after placing the droplet.

(b) Time step 9, 87 min. after placing the droplet.

Fig. 5. Greyscale vertical radial slices of tomogram corresponding to time steps 1 (a) and 9 (b) of the penetrating droplet in sample 2.

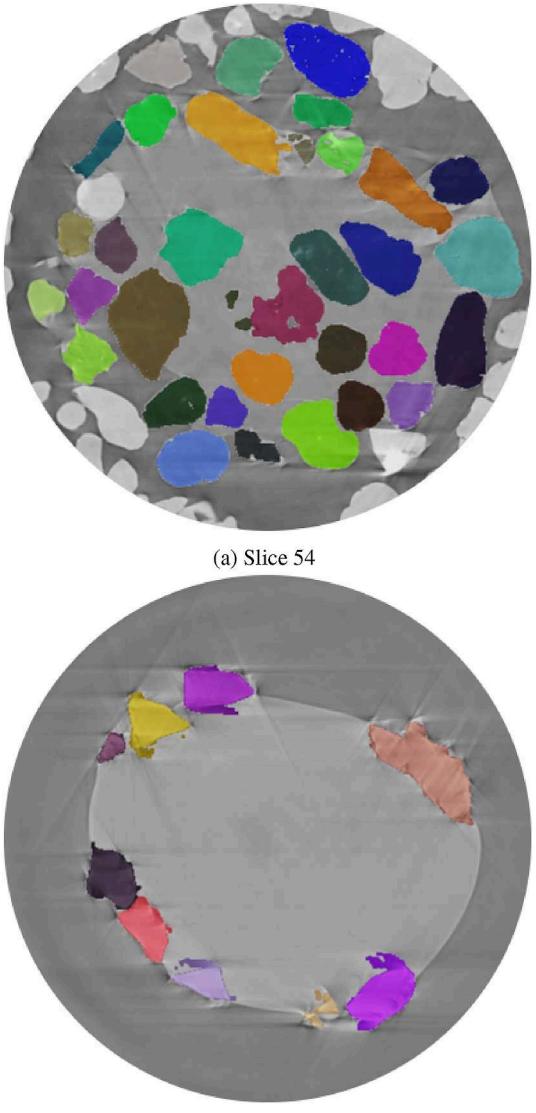

(a) Slice 54

(b) Slice 216

Fig. 6. Two different labelled slices of the first tomogram, one closer to the base of the water droplet (a) and the second closer to its top (b). Motion artefacts are noticeable around some of the borders of the grains. Each colour denotes one different label and therefore, grain.

artefacts present in the image, mostly concentrated in the water phase, a three-dimensional (3D) visualisation of the droplet surrounded by the grains is not sharp enough to be presented.

3.2. Labelled images

Fig. 6 presents the labelled grains in slices 54 and 216 of the first tomogram of sample 1 as an example of the procedure. Each colour denotes one different label and therefore, grain. The top view of the 3D visualisation of those labels is presented in Fig. 7 using the 3D viewer from ImageJ (Schmid et al., 2010; Schindelin et al., 2012). Table 2 summarises the number of labels that did converge later during the DDIC for each tomogram of each sample and thus were tracked, averaging 65 of them for each tomogram of sample 1 and 91 for sample 2. The last tomogram, fifth for sample 1 and ninth for sample 2, do not require labelling because it is only employed as $n+1$ and not as n for the workflow presented in Section 2.4.

3.3. Displacement field

Following the steps described in Section 2.4 for each sample, the displacement field of the labelled grains was created for each pair of consecutive steps, as presented in Figs. 8 and 9. The displacements are represented by the arrows, from which the colours represent the time step. The time step means which consecutive tomogram that data originates from. The arrows are placed in the position of the grain at that time step, which means that the combined arrows show the path of that grain in that plane during the experiment. For the sake of the better visualisation of the displacement paths, the *XZ*- and *YZ*-views, which are the vertical sections, were placed around the *XY*-view, which is the top view.

The units on the axes of Figs. 8 and 9 and the units in which the displacements are measured in are related to the pixels of the images. This means that the units used represent how many pixels the displacement consists of. For both samples the pixel size in one slice is approximately 0.022 mm $\times$ 0.022 mm.

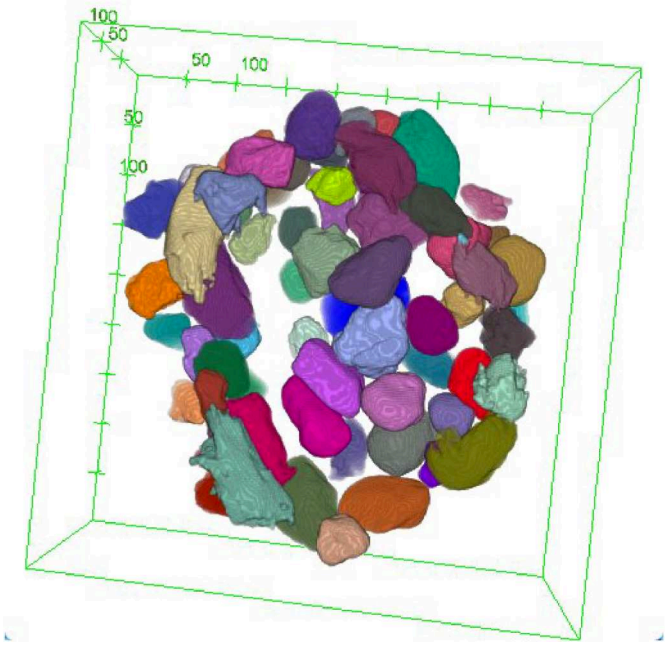

Fig. 7. Top view of a 3D visualisation of the labelled grains for the first time step of sample 1. The scale on the bounding box of the image is in pixels. Each colour denotes one different label and therefore, grain.

Table 2
Number of labels able to converge for each analysed tomogram of each sample.

Tomogram (time steps)	1	2	3	4	5	6	7	8
Labels: sample 1	63	68	58	69	–	–	–	–
Labels: sample 2	92	94	88	95	89	90	95	87

To make Figs. 8 and 9 easier to understand, an estimation of the region occupied by the droplet on the first time step was draw in cyan. This estimation is elaborated based on a convex hull created around combined displacements in that plane also in the first time step that are bigger then a threshold value, which separated grains on the base from grains that are displaced by the interaction with the droplet. Those combined displacements represent the two dimensional vectorial sum of displacements in each of the plots. The estimated droplet in the *XY*-view in Fig. 8 is similar to the position of the droplet observed in Fig. 6a. Also the drawn line in the *XZ*-view in Fig. 8 is similar to the position of the droplet observed in Fig. 4a. The authors chose to extrapolate the estimation of the droplet outside the imaged area to make visualisation clearer. At the estimation of the initial position of the droplet sample 2, in Fig. 9, as the right-hand side of the droplet is not fully in the field of view, this part of the hull was drawn in dashed line and not considered during the creation of the blue region.

Analysing the pattern of displacements, it is noticeable that grains move first upwards towards the top of the droplet (time steps 1 and 2 in Fig. 8 and time steps 1-5 or 6 in Fig. 9) and then, as the droplet starts penetrating, the vertical displacement gets progressively smaller until it changes direction and the grains start moving downwards (time steps 3 and 4 in Fig. 8 and time steps 5 or 6-8 in Fig. 9). In the *XZ*-views of Figs. 8 and 9 it is clear that almost all affected grains are carried progressively slower towards the center of the droplet. The heterogeneous and asymmetric tendencies observed in all the mentioned figures are probably related to the different shapes and sizes of the sand grains.

At the *YZ*-view of Fig. 9, the displacements are not very pronounced because the section cuts the droplet far from its center, meaning that the radial direction is short in this plane, and thus also the displacements. At the *XZ*-view of Fig. 9, on the other hand, those displacements are very pronounced, given that this section is virtually over the center of the droplet.

Analysing Figs. 8 and 9 together, the penetration mechanism of a small water droplet on a hydrophobic substrate is clear, even though the size of the samples is limited. As the droplet slowly penetrates, grains around the triple-line at the droplet's base, where water meets air and grains at the same time, are dragged to its surface, causing them to move upwards and towards the center. As time passes and the droplet penetrates a bit more, those grains

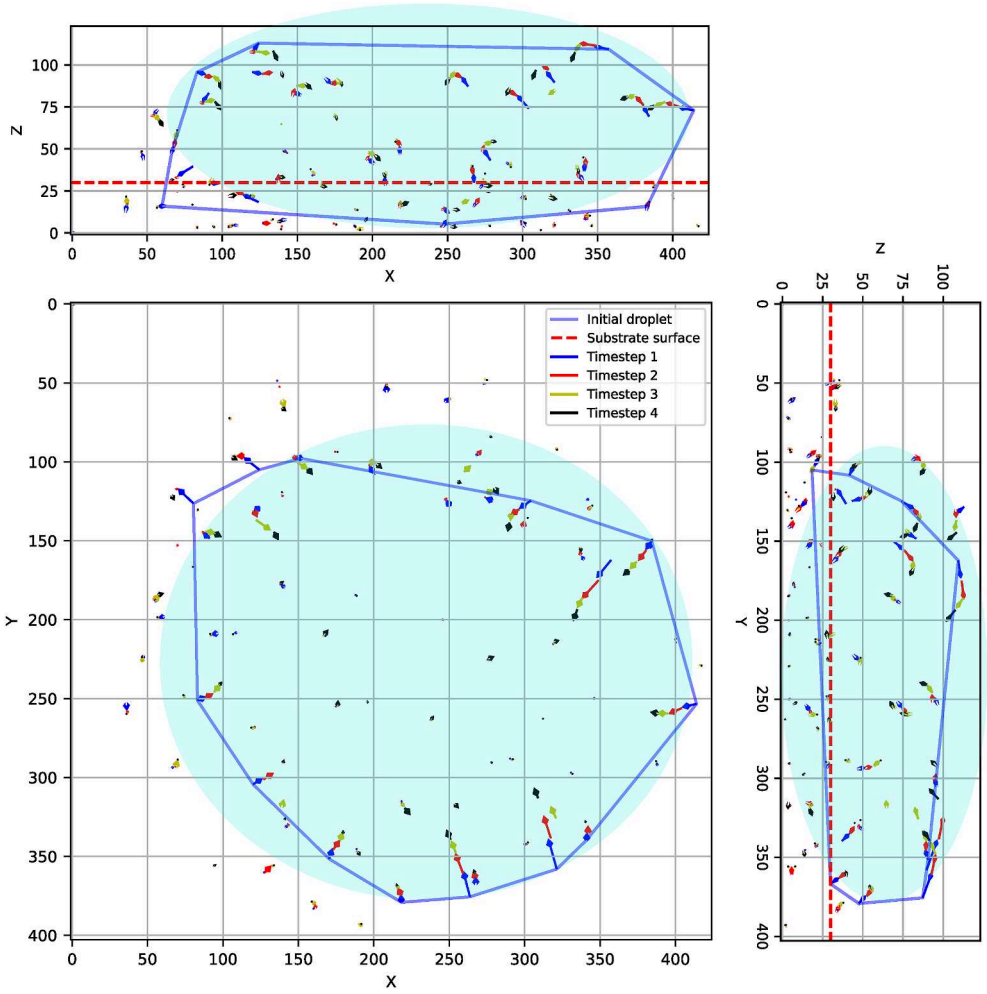

Fig. 8. Displacement of hydrophobic grains of sample 1 during penetration of the droplet viewed from different perspectives, as indicated by the axis of each subplot. The time difference between each step is around 10 min. The axes unit is the amount of pixels that the displacement consists of, each of them with a size of approximately 0.022 mm × 0.022 mm.

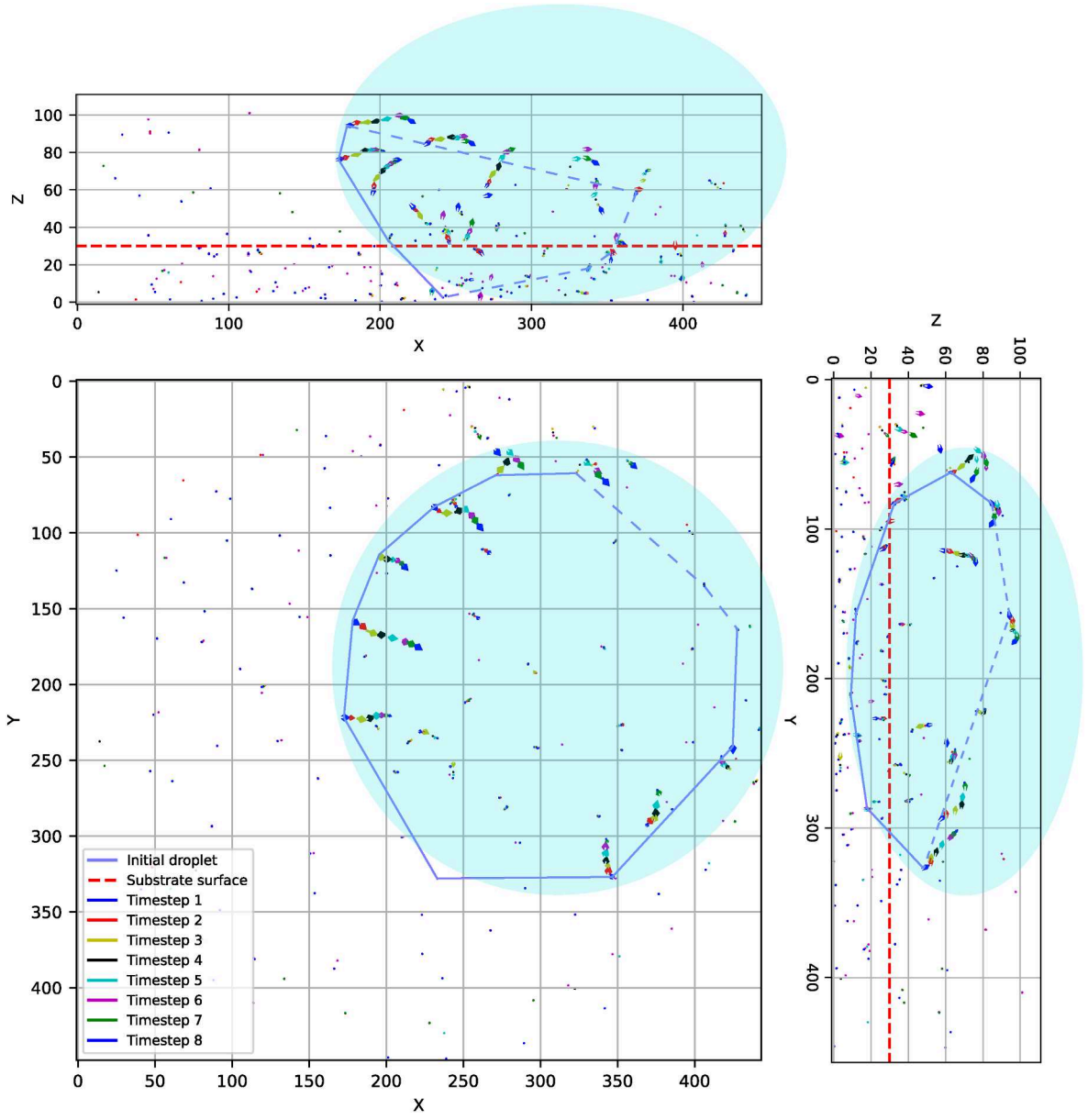

Fig. 9. Displacement of hydrophobic grains of sample 2 during penetration of the droplet viewed from different perspectives, as indicated by the axis of each subplot. The time difference between each step is around 10 min. The axes unit is the amount of pixels that the displacement consists of, each of them with a size of approximately 0.022 mm × 0.022 mm.

are carried by it downwards, inverting the direction of the vertical displacements. The droplet is thus involved by grains of soil as it penetrates the hydrophobic substrate. The grains involve the droplet instead of the droplet involving the grains.

3.4. Displacement statistics

Histograms of the *Z* and *XY* displacements were created for both samples, as presented in Figs. 10 and 11 and also summarised in Table 3. The *XY* displacements are always positive because they consist of the square root of the sum of individual displacements in *X* and *Y* squared.

In Fig. 10a and b, the highest frequency of displacements is concentrated around zero for all time steps, which stems from the grains closer to the base of the sample and that are not in contact with or in the area of influence of the droplet. Comparing the histograms also shows that the relative frequency of this class grows with the passing of time, meaning that less and less grains are moving as the time passed increases.

It is also noticeable in Fig. 10a that the bigger positive *Z* displacements appear more frequently in the first time step, shown in blue in the histogram, than in the second time step, shown in yellow. For this second time step, although positive *Z* displacement values are still present, they are smaller than the ones in the first time step. For the third and fourth time steps, presented respectively in green in red, negative displacements are the ones more frequent, and also the values of those displacements are generally bigger for the last time step. This highlights once again the mechanism in which grains climb around the droplet, then reduce their velocity until they invert their movement direction, and then go down, engulfing the droplet. In Fig. 10b, which is related to the tendency of the grains to move towards a vertical axis through the

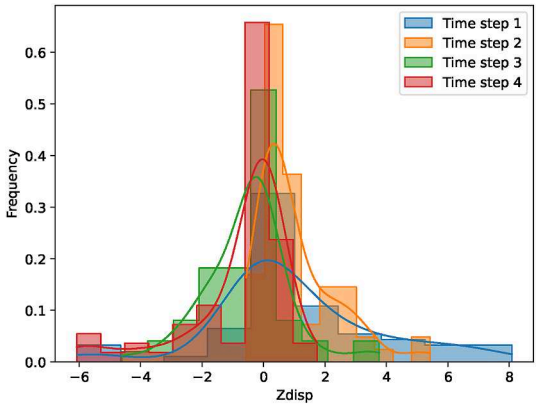

(a) Z-direction displacements.

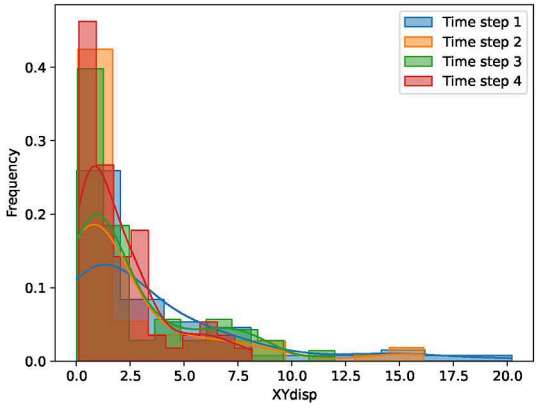

(b) Combined *XY*-direction displacements.

Fig. 10. Histograms of displacements for sample 1.

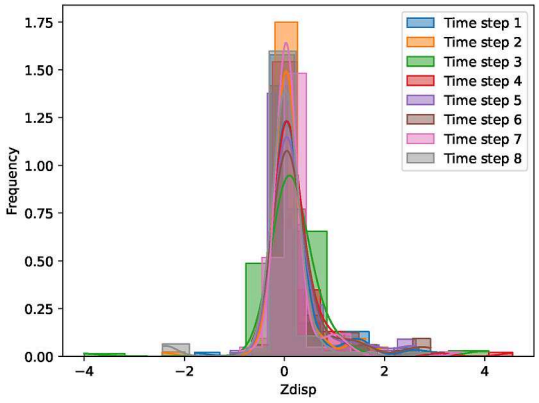

(a) Z-direction displacements.

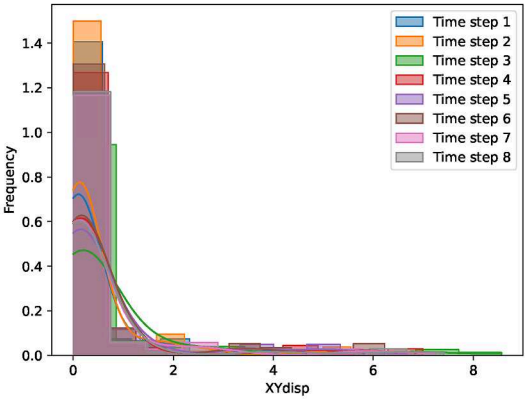

(b) Combined *XY*-direction displacements.

Fig. 11. Histograms of displacements for sample 2.

center of the droplet, it is noticeable that the *XY* displacements get more and more concentrated around zero with the passing of time, meaning that they move faster in the beginning until they progressively reduce their velocity until they stop moving, but now in a different position than that before the droplet was placed.

On the other hand, the histogram of displacements in the *Z*-axis for sample 2, as depicted in Fig. 11a, has a narrower base when compared to Fig. 10a. This means that the absolute values are smaller. They also do not present a clear tendency of positive displacements followed by negative ones as time passes. The histogram in Fig. 11b also has a narrower base then the one in Fig. 10b, meaning that *XY* displacements are also smaller and slower than for sample 1 in the *XY*-plane. For sample 2, then, the mechanism of penetration consists of grouping the grains around the droplet with smaller velocity and absolute displacements. This difference the intensity of the presented mechanism for each case is explained by sample 1 being more hydrophobic than sample 2, according to Section 2.1, and thus resisting the contact with water even more.

For better visualisation and comparison, Fig. 12 was elaborated, in which average *XY* and *Z* displacements are presented separately for each time step and each sample. There it is noticeable once again that the average *XY* displacement of grains in sample 1, represented by black crosses, is significantly higher than that of the grains in sample 2, represented by red crosses. Regarding the average *Z* displacements, sample 1 has more pronounced positive average *Z* displacements in the beginning of the test, followed by an equally pronounced negative average *Z* displacement. The average *Z* displacements of the grains in sample 2, the less hydrophobic one, are comparatively smaller and stay close to zero during the whole period. The cause behind this different behavior among samples was exposed in the paragraph above, that being the difference in the hydrophobicity level of samples.

Table 3
Average (avg.) and standard deviation (std.) for each histogram presented. Unit of displacement (disp.) is pixel size.

Sample	Time step	*Z* disp. avg.	*Z* disp. std.	*XY* disp. avg.	*XY* disp. std.
1	1	1.0290	2.6908	3.6023	4.4002
	2	1.0426	1.2476	2.4705	3.5774
	3	−0.5358	1.3798	2.5714	2.8172
	4	−0.7570	1.6577	1.9823	1.9356
2	1	0.2143	0.6395	0.5169	1.0990
	2	0.1402	0.5135	0.4920	1.0300
	3	0.2255	0.7865	0.8094	1.6541
	4	0.2379	0.6112	0.5845	1.3766
	5	0.2787	0.6253	0.6694	1.3977
	6	0.2968	0.6532	0.6006	1.2756
	7	0.1404	0.4697	0.5795	1.3571
	8	0.0004	0.5907	0.5245	1.4089

To confirm the statistical significance of the observations described above, a linear regression was elaborated for each group of data plotted in Fig. 12 and a F-test was performed to compare the coefficients of these linear regressions. The *p*-value returned by the test between *Z* displacements of both samples is 0.0004449,

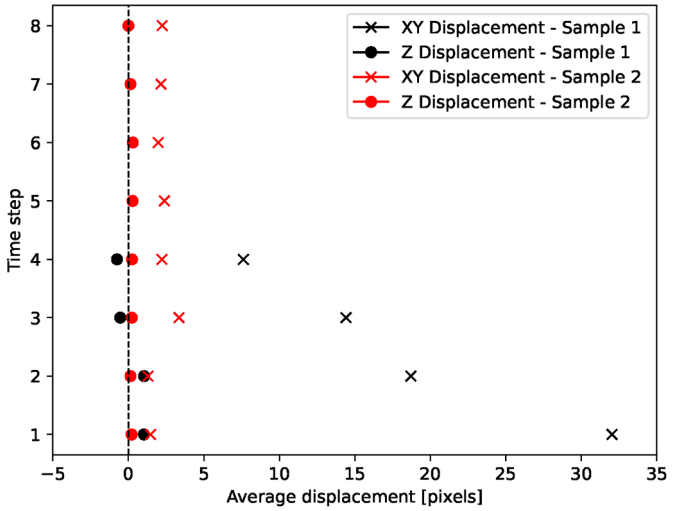

Fig. 12. *XY* and *Z* displacement average at each time step for both samples.

while the one for the test between *XY* displacements is 0.0011466. Since they are both smaller than 0.05, one can reject the null hypothesis and confirm that the displacement tendencies of the samples are different, which probably stems from the difference in the degree of hydrophobicity.

3.5. Visible light imaging

In a similar experiment performed using a regular optical microscope and water coloured with food colouring, it is possible to observe that, while the hydrophobic grains climb the droplet, as already shown, they are not fully covered by water from the droplet, as presented in Fig. 13. The food colouring used for this experiment has shown no effect on the contact angle between the

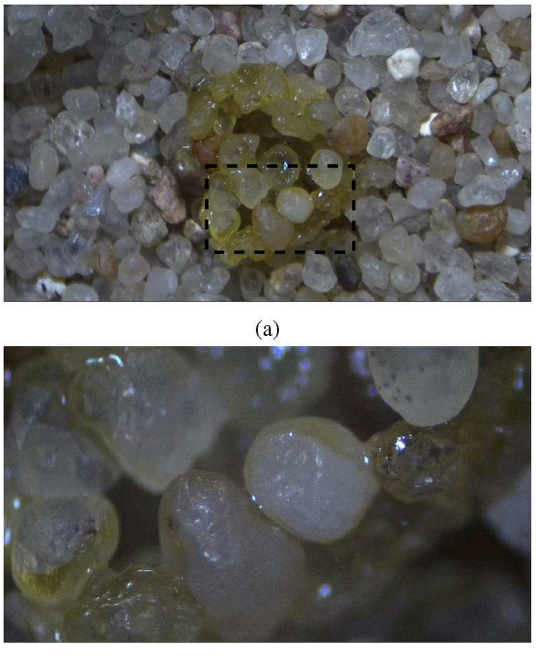

(a)

(b) Zoom on indicated region of (a)

Fig. 13. Hydrophobic grains climbing around a yellow coloured water droplet placed on the hydrophobic sand surface moments before being viewed, viewed by an optical microscope. The surface of the grains is not fully covered by water.

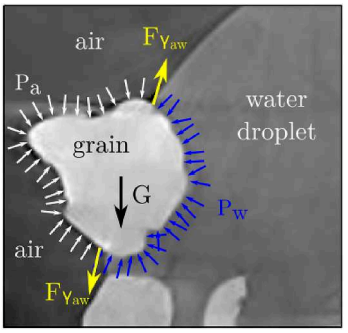

Fig. 14. The 2D free-body diagram of forces acting on a specific sand grain. The forces are not up to scale and were only drawn for one grain in the figure, although they also exist for the other ones. The background is the greyscale CT image presented on Fig. 4.

liquid, solid and air. Unfortunately, this thin water film would not be segmentable in the previous CT images and thus we cannot confirm that the partial liquid coverage also happened during that experiment due to strong motion artefacts on the top of the sample.

For the more commonly encountered hydrophilic sands, the mechanism is completely different. There, water rapidly involves the grains and penetrates the substrate in less than seconds, as there is no resistance of the grain surface to coming into contact with water, but rather an attraction. Given the velocity with which water penetrates hydrophilic substrate, it was not possible to image the behaviour and thus it was observed only in the laboratory to enable the comparison.

3.6. Analytics of the phenomena

The surface tension between the hydrophobically coated grains and water is high, leading to a minimization of this unfavourable contact surface between both and also to grains not being fully covered in water. The interplay between internal fluid cohesion and fluid-solid adhesion determines interrelated properties like surface tension between water and air (γ_{aw}), liquid and gas pressure, contact angle, and the general functioning of the phenomena. The difference between air (P_a) and water (P_w) pressure is known as suction and can be calculated by Eq. (1), in which the radius ($\bar{r}$) represents the average curvature of the water structure (Willett et al., 2007). The surface tension force ($F_{\gamma_{aw}}$) is parallel to the liquid surface where contact happens and pressure is normal to the surface. Eq. (2) allows for the calculation of this force (Sophocleous, 2010). There, θ is the contact angle and L is the length of the triple line, which can be approximated when considering the average grain radius, $\bar{r}_{grain}$. The free-body diagram of the acting forces on one grain is presented in Fig. 14, in which G represents the gravity force. The colours are merely illustrative and their use aim at making the figure easier to understand. The resultant force of these individual forces causes the displacements described in this paper.

$$\Delta P = P_a - P_w = \gamma_{aw} \frac{1}{\bar{r}} \tag{1}$$

$$F_{\gamma_{aw}} = \gamma_{aw} L \cos\theta = \gamma_{aw} 2\pi \bar{r}_{grain} \cos\theta \tag{2}$$

4. Conclusions

This paper investigates in detail and quantitatively the

mechanism of the soil-water interaction while a droplet penetrates a hydrophobic sand substrate in two different experiments. It is observed that grains climb around the droplet while they are still not fully in contact with the liquid, as indicated by optical microscope image and CT images and the respective displacement field of the imaged grains. Their displacement is upwards in the beginning, climbing around the droplet, until the liquid starts carrying them downwards while penetrating. From the top view it is noticeable that the grains move towards the center of the droplet. This phenomenon is contrary to what is observed in hydrophilic soils, in which the fluid quickly involves the grains and penetrates into the pore space between them without significant grain displacement. The major goal of the study is to improve the fundamental and general understanding of water penetration in hydrophobic substrates, which can lead to a better design and application of those.

The paper also presents a comparison between the described mechanism happening in two different samples, which have different hydrophobicity levels. It was observed that the more hydrophobic grains from sample 1 had more and faster displacements, both in the *Z*- and *XY*-planes. For them, the *Z*-direction upward displacement followed by respective downward one is more evident. For the less hydrophobic grains of sample 2, they mostly moved upwards, but with a smaller modulus, and clumped around where the center of the droplet once was.

The future direction of this research includes the observation of the effect of temperature, droplet size, and grain shape on the described phenomena. Temperature can affect the viscosity of fluids and thus the surface tension involved, while grain shape and surface roughness can alter the pinning of the triple-line on the solid and thereby influence contact angle. Those changes to the individual terms causing the observed phenomenon will alter the interplay between them and thus maybe the final outcome, which will be investigated in a future stage. The volume of the droplet is also of interest, since there is probably a limit to the height the grains will be elevated to. Those future results can lead to better understanding of hydrophobic materials and their applications and also to their optimization. Numerical modelling is also to be employed, and for that a method that is able to capture both the hydraulic and mechanical expressions of the phenomenon must be chosen, of which an example is the lattice Boltzmann method (LBM) coupled to the discrete element method (DEM).

CRediT authorship contribution statement

Clara M. Toffoli: Writing – review & editing, Writing – original draft, Visualization, Validation, Software, Methodology, Investigation, Formal analysis, Data curation, Conceptualization. **Marius Milatz:** Writing – review & editing, Supervision, Investigation, Funding acquisition. **Julian P. Moosmann:** Writing – review & editing, Investigation. **Thomas Jentschke:** Writing – review & editing, Methodology. **Felix Beckmann:** Funding acquisition. **Jürgen Grabe:** Funding acquisition.

Declaration of competing interest

The authors declare that they have no known competing financial interests or personal relationships that could have appeared to influence the work reported in this paper.

Acknowledgements

The authors acknowledge the funding of this research by the German Research Foundation (Deutsche Forschungsgemeinschaft, DFG) in the framework of Research Training Group GRK 2462: Processes in natural and technical Particle-Fluid-Systems at Hamburg University of Technology (TUHH).

We acknowledge the Deutsches Elektronen-Synchrotron DESY (Hamburg, Germany), a member of the Helmholtz Association HGF, for the provision of experimental facilities. Parts of this research were carried out at PETRA III. Beamtime was allocated for proposal 20220840. This research was supported in part through the Maxwell computational resources operated at DESY and by the project Holistic Data Analysis (HoliDAy) of the Innovation-, Information-& Biologisation-Fonds (I2B) of Hereon.

References

Adams, S., Strain, B., Adams, M., 1970. Water-repellent soils, fire, and annual plant cover in a desert scrub community of southeastern California. Ecology (51), 696–700.
Ahmad, D., Van Den Boogaert, I., Miller, J., Presswell, R., Jouhara, H., 2018. Hydrophilic and hydrophobic materials and their applications. Energy Sources: Recovery Util. Environ. Eff. (40), 2686–2725.
Al-Atroush, M., Sebaey, T., 2021. Stabilization of expansive soil using hydrophobic polyurethane foam: a review. Transp. Geotech. (27), 100494
Bachmann, J., Ellies, A., Hartge, K., 2000. Development and application of a new sessile drop contact angle method to assess soil water repellency. J. Hydrol. 231, 66–75.
Bardet, J.P., Jesmani, M., Jabbari, N., 2014. Permeability and compressibility of wax-coated sands. Geotechnique (64), 341–350.
Bayad, M., Chau, H.W., Trolove, S., Moir, J., Condron, L., Bouray, M., 2020. The relationship between soil moisture and soil water repellency persistence in hydrophobic soils. Water (12), 2322.
Bisdom, E., Dekker, L., Schoute, J.T., 1993. Water repellency of sieve fractions from sandy soils and relationships with organic material and soil structure. In: Soil Structure/soil Biota Interrelationships. Elsevier, pp. 105–118.
Dauchy, X., 2023. Evidence of large-scale deposition of airborne emissions of per- and polyfluoroalkyl substances (pfass) near a fluoropolymer production plant in an urban area. Chemosphere 337, 139407.
DeBano, L.F., 1981. Water Repellent Soils: a State-Of-The-Art, vol. 46. US Department of Agriculture, Forest Service. Pacific Southwest Forest and Range Experiment Station.
Doerr, S.H., Shakesby, R.A., Walsh, R.P., 1996. Soil hydrophobicity variations with depth and particle size fraction in burned and unburned eucalyptus globulus and pinus pinaster forest terrain in the águeda basin, Portugal. Catena (27), 25–47.
Doerr, S.H., 1998. On standardizing the 'Water Drop Penetration Time' and the 'Molarity of an Ethanol Droplet' techniques to classify soil hydrophobicity: a case study using medium textured soils. Earth Surf. Process. Landf. (23), 663–668.
Hall, S.A., 2012. Digital image correlation in experimental geomechanics. ALERT Geomater. Dr. Summer Sch. 69–102, 2012.
Henry, B.J., Carlin, J.P., Hammerschmidt, J.A., Buck, R.C., Buxton, L.W., Fiedler, H., Seed, J., Hernandez, O., 2018. A critical review of the application of polymer of low concern and regulatory criteria to fluoropolymers. Integr. Environ. Assess. Manag. (14), 316–334.
Karatza, Z., Buckman, J., Medero, G.M., Beckett, C.T., 2021. Evolution of meniscus structures in hydrophobic granular systems. J. Hydrol. 603, 126954.
Keley, M.M., 2017. Super-hydrophobic Surfaces Based on Fluorinated Carbon and its Application on Avoiding Ice-Accretion. Universidade Federal do Rio de Janeiro. Ph.D. thesis.
Legland, D., Arganda-Carreras, I., Andrey, P., 2016. MorphoLibJ: integrated library and plugins for mathematical morphology with ImageJ. Bioinformatics (32), 3532–3534.
Lin, H., Lourenço, S.D., 2020. Physical degradation of hydrophobized sands. Powder Technol. 367, 740–750.
Liu, D., Lourenço, D.S., Yang, J., 2019a. Critical state of polymer-coated sands. Geotechnique (69), 841–846.
Liu, D., Sandeep, C., Senetakis, K., Nardelli, V., Lourenço, S., 2019b. Micromechanical behaviour of a polymer-coated sand. Powder Technol. 347, 76–84.
Liu, D., Lourenço, S.D., 2021. Stress-dilatancy behaviour of a polymer-coated sand. Acta Geotech (16), 647–652.
Lourenço, S.D.N., Woche, S.K., Bachmann, J., Saulick, Y., 2015. Wettability of crushed air-dried minerals. Géotech. Lett. (5), 173–177. Publisher: ICE Publishing.
Lourenço, S., Saulick, Y., Zheng, S., Kang, H., Liu, D., Lin, H., Yao, T., 2018. Soil wettability in ground engineering: fundamentals, methods, and applications. Acta Geotech (13), 1–14.
Maciejewski, H., Karasiewicz, J., Dutkiewicz, M., Marciniec, B., 2015. Hydrophobic materials based on fluorocarbofunctional Spherosilicates. Silicon (7), 201–209.
Magens, O.M., Liu, Y., Hofmans, J.F., Nelissen, J.A., Wilson, D.I., 2017. Adhesion and cleaning of foods with complex structure: effect of oil content and fluoropolymer coating characteristics on the detachment of cake from baking surfaces. J. Food Eng. 197, 48–59.
Ma'shum, M., Farmer, V., 1985. Origin and assessment of water repellency of a sandy south australian soil. Soil Res. (23), 623–626.

Matsuoka, Y., Iida, O., Suemitsu, K., Oka, K., Ota, N., Izumi, M., 2021. Use of a fluoropolymer-based paclitaxel-eluting stent for arteriovenous graft outflow vein stenosis in hemodialysis patients. J. Vasc. Surg. Cases Innov. Tech. (7), 326–331.
McGhie, D., Posner, A., 1981. The effect of plant top material on the water repellence of fired sands and water repellent soils. Aust. J. Agric. Res. (32), 609–620.
Milatz, M., Hüsener, N., Andò, E., Viggiani, G., Grabe, J., 2021. Quantitative 3d imaging of partially saturated granular materials under uniaxial compression. Acta Geotech (16), 3573–3600.
Moosmann, J., Ershov, A., Weinhardt, V., Baumbach, T., Prasad, M.S., LaBonne, C., Xiao, X., Kashef, J., Hofmann, R., 2014. Time-lapse X-ray phase-contrast microtomography for in vivo imaging and analysis of morphogenesis. Nat. Protoc. (9), 294–304.
Moosmann, J., 2019. Data Reconstruction and Analysis Tools for Tomography Data Acquired at the P05 Imaging Beamline (Ibl) and the P07 High-Energy Material Science (Hems) Beamline at Petra Iii at Desy github.com/moosmann/matlab.
Roberts, F., Carbon, B., 1971. Water Repellence in Sandy Soils of South-Western Australia: 1. Some Studies Related to Field Occurrence. Field Station Record 10. Division of Plant Industry. CSIRO, Australia.
Sandor, R., Iovino, M., Lichner, L., Alagna, V., Forster, D., Fraser, M., Kollár, J., Šurda, P., Nagy, V., Szabo, A., et al., 2021. Impact of climate, soil properties and grassland cover on soil water repellency. Geoderma 383, 114780.
Schindelin, J., Arganda-Carreras, I., Frise, E., Kaynig, V., Longair, M., Pietzsch, T., Preibisch, S., Rueden, C., Saalfeld, S., Schmid, B., Tinevez, J.Y., White, D.J., Hartenstein, V., Eliceiri, K., Tomancak, P., Cardona, A., 2012. Fiji: an open-source platform for biological-image analysis. Nat. Methods (9), 676–682.
Schmid, B., Schindelin, J., Cardona, A., Longair, M., Heisenberg, M., 2010. A high-level 3d visualization api for java and imagej. BMC Bioinf. 11, 1–7.
Schroeter, B., Jung, I., Bauer, K., Gurikov, P., Smirnova, I., 2021. Hydrophobic modification of biopolymer aerogels by cold plasma coating. Polymers (13), 3000.
Shahraeeni, E., Or, D., 2012. Pore-scale evaporation-condensation dynamics resolved by synchrotron x-ray tomography. Phys. Rev. E: Stat., Nonlinear, Soft Matter Phys. (85), 016317
Sophocleous, M., 2010. Understanding and explaining surface tension and capillarity: an introduction to fundamental physics for water professionals. Hydrogeol. J. (18), 811.
Stamati, O., Andò, E., Roubin, E., Cailletaud, R., Wiebicke, M., Pinzón, G., Couture, C., Hurley, R., Caulk, R., Caillerie, D., Matsushima, T., Bésuelle, P., Bertoni, F., Arnaud, T., Ortega Laborin, A., Rorato, R., Yue, S., Tengattini, A., Okubadejo, O., Birmpilis, G., 2020. Spam: software for practical analysis of materials. J. Open Source Softw. (5), 2286.
Teng, H., 2012. Overview of the development of the fluoropolymer industry. Appl. Sci. (2), 496–512.
Thepaksorn, P., Lee, P., Shiwaku, Y., Zheng, B., Koizumi, A., Harada, K.H., 2023. Formation and degradability of per-and polyfluoroalkyl substances in river soils around a fluoropolymer-manufacturing plant in osaka, Japan. Arch. Environ. Contam. Toxicol. 1–9.
Toffoli, C.M., Milatz, M., Grabe, J., 2023. On the resistance of hydrophobic soil polymer coatings created by cold plasma polymerization. E3S Web Conf. 382, 18003.
Toffoli, C.M., Milatz, M., Moosmann, J., Jentschke, T., Beckmann, F., 2024. Synchrotron Ct Images of Hydrophobic Sand: 1. Wetting via Droplet Condensation and 2. Water Drop Penetration Time Test. https://doi.org/10.15480/882.8774. URL:
Wang, W., Zhang, Y., Li, H., 2021. Quantification of soil structure via synchrotron x-ray tomography after 22 years of fertilization. Eur. J. Soil Sci. (72), 2115–2127.
Wijewardana, N.S., Kawamoto, K., Moldrup, P., Komatsu, T., Kurukulasuriya, L.C., Priyankara, N.H., 2015. Characterization of water repellency for hydrophobized grains with different geometries and sizes. Environ. Earth Sci. (74), 5525–5539.
Willett, C.D., Johnson, S.A., Adams, M.J., Seville, J.P., 2007. Pendular capillary bridges. In: in: Handbook of Powder Technology, 11, pp. 1317–1351. Elsevier.
Yang, B., Jiang, S., Huang, J., Hao, M., Zhang, T., Ramakrishna, S., Liu, Y., 2023. Applications of fluoropolymer nanocomposites in textile industry. In: Advanced Fluoropolymer Nanocomposites. Elsevier, pp. 719–754.
Zainal, M.N.F., Redzuan, N., Misnal, M.F.I., 2015. Brief review: cold plasma. Jurnal Teknologi (74).
Zheng, S., Xing, X., Lourenço, S.D.N., Cleall, P.J., 2021. Cover systems with synthetic water-repellent soils. Vadose Zone J. (20), e20093

Clara M. Toffoli is currently working on her PhD thesis at the Hamburg University of Technology (TUHH), Germany, since 2022. She completed her bachelor's and master's degrees at the University of Brasilia (UnB), Brazil. Her current research includes experiments on hydrophobic soils and also numerical modelling of partially saturated granular media via lattice Boltzmann method (LBM).